PHYSICAL REVIEW B VOLUME 60, NUMBER 16 15 OCTOBER 1999-II

Excited-state absorption spectroscopy of Er^{3+}-doped $Y_3Al_5O_{12}$, YVO_4, and phosphate glass

P. Le Boulanger, J.-L. Doualan,* S. Girard, J. Margerie, and R. Moncorgé
Centre Interdisciplinaire de Recherche Ions Lasers, UMR 6637, CEA-CNRS-ISMRA, Université de Caen,
6, Boulevard Maréchal Juin, 14050 Caen Cedex, France

(Received 28 April 1999)

The spectra of excited-state absorption (ESA) and stimulated-emission (SE) cross sections of Er^{3+} in $Y_3Al_5O_{12}$, YVO_4, and phosphate glass have been registered between 0.4 and 3 μm with a pump and probe technique. The experimental setup, based on the use of cw light sources, is described in detail. The incidence of ESA on the laser properties of these Er^{3+}-doped oxide hosts is evaluated particularly around 0.55, 1.6, and 2.8 μm, corresponding to the ${}^4S_{3/2}\rightarrow{}^4I_{15/2}$, ${}^4I_{13/2}\rightarrow{}^4I_{15/2}$, and ${}^4I_{11/2}\rightarrow{}^4I_{13/2}$ laser transitions, respectively. The migration $[({}^4I_{13/2},{}^4I_{15/2})\rightarrow({}^4I_{15/2},{}^4I_{13/2})]$ and up-conversion $[({}^4I_{13/2},{}^4I_{13/2})\rightarrow({}^4I_{9/2},{}^4I_{15/2})]$ energy transfers involved in some laser operations are analyzed by deducing the energy-transfer microparameters C_{DD} and C_{DA} from ESA and SE measurements. The Judd-Ofelt analysis, usually applied from the ground-state manifold, is then used to evaluate the ESA integrated cross sections and these calculated cross sections are found equal to the measured ones within about 20%. [S0163-1829(99)08539-2]

INTRODUCTION

Trivalent rare earths are the most used active ions in solid-state laser devices.[1] Among them, Er^{3+} provides interesting laser emissions, for example, around 1.5 μm for eye-safe or telecommunication applications (${}^4I_{13/2}\rightarrow{}^4I_{15/2}$ optical transition) and around 2.9 μm for medical purposes (${}^4I_{11/2}\rightarrow{}^4I_{13/2}$). Most of the trivalent rare-earth ions (RE^{3+}) have numerous energy levels and many of them are characterized by long lifetimes leading to intermanifolds radiative transitions with large energy storage capabilities. Consequently, excited-state absorption (ESA) is an important issue both because it can be very detrimental when it occurs at the pump or at the laser emission wavelengths and because it is useful in up-conversion pumping schemes involving intermediary energy levels [${}^4S_{3/2}\rightarrow{}^4I_{15/2}$ green laser emission was obtained for example at 561 and 551 nm in Er^{3+}-doped $Y_3Al_5O_{12}$ (YAG) and $LiYF_4$ (YLF) crystals following such an excited-state-absorption up-conversion process[2]]. On the other hand, high doping ion concentrations (a few atomic percent) are often necessary to compensate for the low oscillator strengths of these $4f$-$4f$ parity forbidden optical transitions. In these conditions, strong multipolar interactions and energy transfers occur between the RE^{3+} active ions;[3] some of them can be useful and others detrimental, as for ESA. Laser emissions around 2.8–2.9 μm (${}^4I_{11/2}\rightarrow{}^4I_{13/2}$ Er^{3+} transition) of highly doped systems such as Er:YAG or Er:YLF are good examples of the complexity of such excitation mechanisms. It is precisely because of these up-conversion energy transfers that laser emission of Er:YAG at 2.94 μm could be observed after pumping into the ${}^4I_{13/2}$ terminal level of the laser transition.[4] As a matter of fact, due to this complexity, and also because they may not only depend on the ion populations in the involved ground and excited levels but also on the ion distributions inside the host matrices, the energy-transfer parameters are often difficult to evaluate from rate equations and fits to fluorescence data. An interesting alternative consists in calculating the microparameters for energy transfers between adjacent active ions and describing the macroscopic effects by using statistical models. The energy-transfer microparameters indeed involve overlap integrals[5] either between emission and ground-state absorption cross-section spectra in case of regular energy transfers or between emission and excited-state absorption cross-section spectra in case of up-conversion mechanisms. The ground-state absorption and the emission cross-section spectra can be directly obtained by using conventional techniques. ESA spectra can be obtained indirectly from the emission profiles corresponding to the reverse optical transitions and by using the so-called reciprocity method. However, this procedure only applies for a restricted number of intermanifold transitions and requires the exact knowledge of specific parameters such as the radiative lifetime and the branching ratio of the involved energy levels. Use can be made also of the Judd-Ofelt (JO) formalism[6,7] and of the JO parameters which can be derived from the analysis of the ground-state absorption spectra (GSA). In this case, only approximative values of integrated cross sections of intermultiplet transitions can be obtained without any information on the associated spectral profile. Direct registrations of detailed and complete ESA cross-section spectra are thus considerably more informative but they require much more care, and an especially dedicated experimental setup based on a pump-probe technique is necessary. The pump beam has to be a laser to bring enough ions into the selected absorbing excited level. The probe beam is either a tunable laser or a lamp. In case of a laser probe, excited-state excitation (ESE) spectra are often preferred,[8] in particular because it is a very sensitive method which allows to obtain spectra more easily. The probe laser brings the already excited ions into an upper excited level from which they relax either radiatively or nonradiatively down to another emitting level. The ESE spectra are thus obtained by scanning the wavelength of the tunable laser probe while monitoring the emitted photons. These spectra have good spectral resolution, that in fact of the laser probe, but they are restricted to particular ESA transitions and they have to be calibrated in the unit of the ESA cross section by using the JO formalism; they are thus only ap-

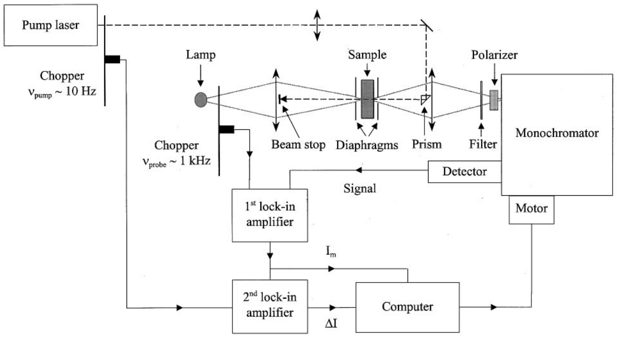

FIG. 1. Excited-state absorption setup based on pump and probe technique.

proximative. The use of a broadband light source probe such as a tungsten-halogen or a xenon lamp is more universal. In this case, the probe beam passes through the sample to be studied and is dispersed and analyzed by a monochromator. The measurements consist then in the registration of differential transmission spectra which allow to obtain at the same time the ESA, the stimulated emission (SE) and the GSA spectra, the latter being used to calibrate the former.

The present paper is dedicated to a complete analysis of the ESA properties of three important Er doped laser materials, Er:YAG, Er:YVO$_4$, and Er:phosphate glass (from Kigre), by using the very efficient pump-probe technique of Koetke and Huber[9] based on two cw light sources, a pump laser and a probe lamp, each beam being modulated at a different frequency and the signal being processed by a cascade of two lock-in amplifiers. The experimental conditions are presented in Sec. I. Section II is devoted to the description and analysis of the ESA spectra. The spectroscopic results are then used in Sec. III to discuss the effect of ESA on the known or potential laser properties of the materials and in Sec. IV to estimate some important energy-transfer microparameters. The data are finally confronted in Sec. V with the predictions of the Judd-Ofelt formalism.

I. EXPERIMENTAL CONDITIONS

The ESA experimental setup, similar to the one of Ref. 9, is shown in Fig. 1. As mentioned above, it is based on a cw pump-probe technique. The laser pump beam is focused into the samples with a spot size of about 150-μm diam (full width at half maximum—FWHM). The laser excitation lines were chosen according to the absorption spectra of the samples and to the wavelength domain to be investigated. The present study was performed in Er^{3+}:YAG, YVO$_4$, and phosphate glass materials, i.e., in oxide materials characterized by high phonon frequencies. Consequently, in these hosts, the multiphonon relaxation between the different energy levels is so rapid that only the lowest metastable level $^4I_{13/2}$ is significantly populated, whatever the excitation wavelength could be (at least in the red and in the near infrared), an approximation which will be made and justified in the following. Moreover, the chosen Er^{3+} dopant concentrations in YAG, YVO$_4$, and in the phosphate glass were 2.8×10^{20}, 4.3×10^{20}, and $2.8\times10^{20}\,\mathrm{cm}^{-3}$, respectively. These dopant concentrations represent a good compromise between a high concentration, thus a high pumping efficiency, and a low concentration to reduce the interion energy-transfer processes. As a matter of fact, as shown in Fig. 2, the $^4I_{13/2}$ manifold could be populated very efficiently, but indirectly, after excitation of higher lying excited levels located in the green and the red with the aid of the blue lines (488.0, 496.5, and 514.5 nm) of an Ar$^+$ laser (Spectra Physics, model 2040) or the red one (647.1 nm) of a Kr$^+$ laser (Coherent, model 70K), the pump powers being maintained around 1 W. The mean population of ions in the excited levels thus produced was typically of the order of a few percent of the dopant concentration. On the other hand, the probe light was provided by a 100-W tungsten-halogen lamp source which delivered a low but very stable signal. The pump and the probe beams were collinear and counterpropagating, the probe

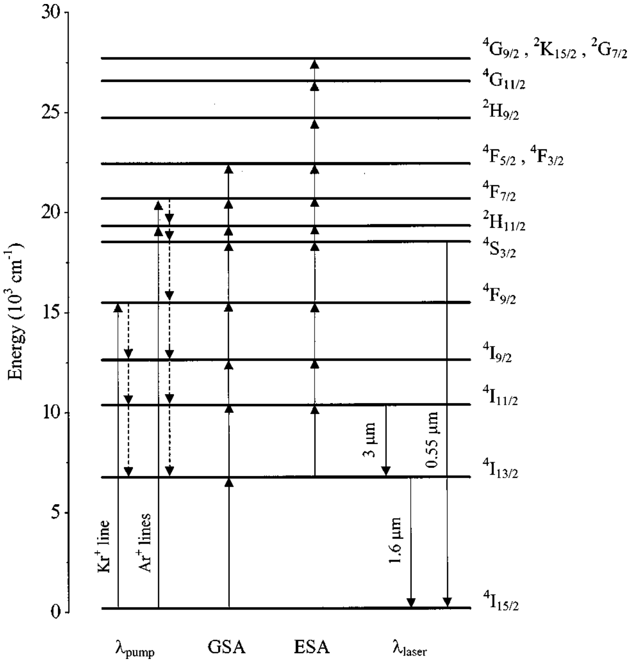

FIG. 2. Energy level diagram of Er^{3+}. The nonradiative transitions are indicated by dotted arrows.

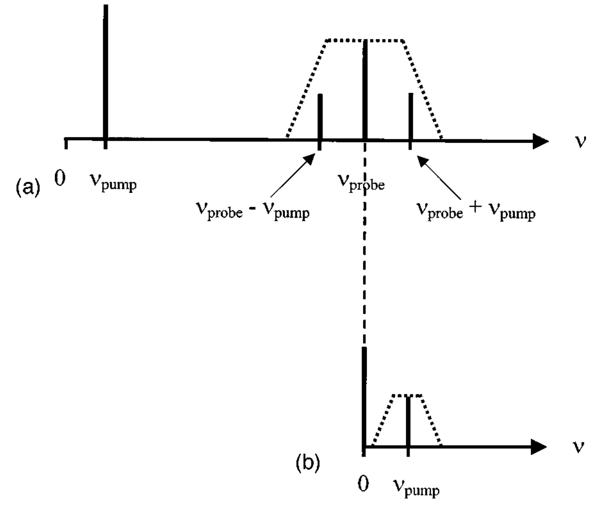

FIG. 3. Principle of the double modulation using a cascade of two lock-in amplifiers. (a) Role of the first lock-in amplifier ($\nu_{probes}\sim1$ kHz). (b) Role of the second lock-in amplifier ($\nu_{pump}\sim10$ Hz).

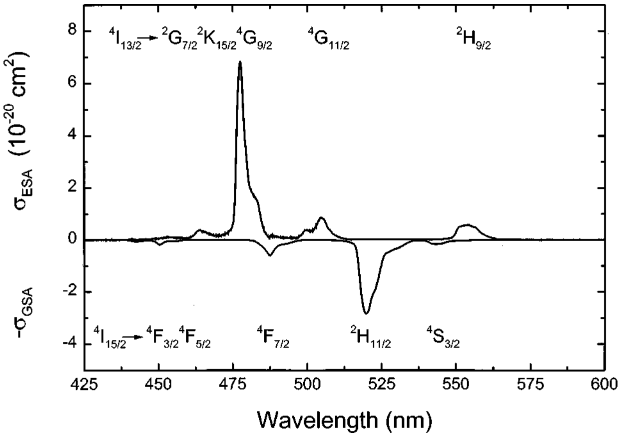

FIG. 4. ESA and GSA spectra of Er^{3+} in phosphate glass (the resolution is 3 Å).

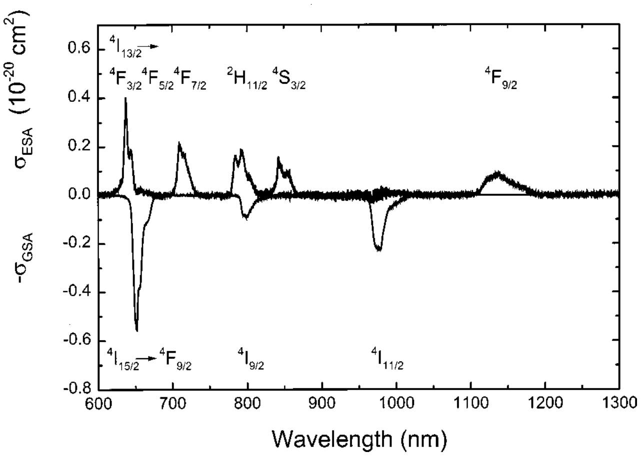

FIG. 5. ESA and GSA spectra of Er^{3+} in phosphate glass (the resolution is 3 Å below 750 nm and 6 Å above).

beam diameter inside the crystal being larger than the pump one. The pump was injected with the aid of a small prism, which also stops the pump light reflected back by the crystal. On each face of the crystal two diaphragms were used to allow a good overlap of the pump and probe beams. A beam stop also prevents the pump beam from reaching the filament of the lamp after passing through the sample. Without this beam stop we observed strong perturbations of the signal during the measurements. Two phenomena were invoked to explain these parasitics: first, the laser beam probably modifies the lamp emission at the pump modulation frequency and second, the pump light reflected on the surface of the lamp envelope is likely to excite again the sample after remodulation at the probe frequency. The wavelength selection was performed with the help of a 0.6-m focal length monochromator (Jobin-Yvon, model HRS2) equipped with three different gratings to cover the near UV to the near IR spectral domain. The detectors used in the experiments were either a photomultiplier (Hamamatsu, model R3896) for the near UV and visible domain, In$_x$Ga$_{1-x}$As photodiodes (Hamamatsu, models G5832-23 and G5852-21) for the IR region up to 2 μm and an InSb photodiode cooled at liquid nitrogen temperature (Judson, model J10-D) for the longer wavelengths up to 3 μm. High gain preamplifiers were specially designed to compensate for the low intensity signal of the probe beam. In the case of the birefringent YVO$_4$ single crystal, a Glan-Thompson polarizer made of calcite was placed in front of the entrance slit of the monochromator to register polarized spectra. The probe beam transmission variations induced by the pump were generally very weak compared to the probe light intensity transmitted by the sample, typically of the order of 10^{-3} to 10^{-5} times smaller. The frequency modulations were provided by two mechanical choppers without phase relationship. The lifetime of the ^{4}I$_{13/2}$ metastable level is very long (a few ms) so that, to achieve a strong rate modulation of its population, the modulation frequency was chosen low ($\nu_{\text{pump}} \sim 10$ Hz). Concerning the probe frequency ($\nu_{\text{probe}} \sim 1$ kHz) the only limitation was the time response of the detectors and of the amplifiers. In these conditions, if we assume, in first approximation, a sinusoidal modulation of the pump and probe beams, the frequency spectrum (see Fig. 3) shows a strong signal at ν_{pump} due to the fluorescence induced by the pump laser and another strong signal at ν_{probe} from the probe modulation. Two weak signals due to the variation of the probe transmission induced by the laser pump also appear at $\nu_{\text{probe}} \pm \nu_{\text{pump}}$. So, the ‘‘difference’’ signals can be measured by using two lock-in amplifiers placed in series. In practice, the first one (Stanford Research Systems, model SR510) is locked at ν_{probe} with a low time constant and provides the mean transmission intensity I_m. The signal at ν_{pump} is eliminated and the signals at $\nu_{\text{probe}} \pm \nu_{\text{pump}}$ passing through this first lock-in amplifier are shifted in frequency by $-\nu_{\text{probe}}$. The second lock-in amplifier (Princeton Applied Research, model PAR 128A), locked at ν_{pump} then measures the transmission variation ΔI induced by the pump. At each wavelength, a computer acquires the two values ΔI and I_m (the time of acquisition depending on the signal-to-noise ratio) and provides the measured signal $(\Delta I/I_m)_{\text{exp}}$.

Let us establish the relationship between this measurement and the cross sections. If I_{off} and I_{on} are the intensity of the probe signal when the pump is off and on, respectively, the following relationships stand between the ground-state absorption, stimulated emission, and excited-state absorption cross sections, σ_{GSA}, σ_{SE}, and σ_{ESA}, respectively,

$$I_{\text{off}} = I_0 e^{-\sigma_{\text{GSA}} N_t L}, \tag{1}$$

$$I_{\text{on}} = I_0 \times \sum_i \gamma_i e^{-\sigma_{\text{GSA}} N_t (L - L_i) - \sigma_{\text{GSA}} (N_t - N_2) L_i - \sigma_{\text{ESA}} N_2 L_i + \sigma_{\text{SE}} N_2 L_i}, \tag{2}$$

the summation being over all the propagation directions of the optical rays with $\Sigma_i \gamma_i = 1$. N_t is the total population density of ions, N_2 the effective ^{4}I$_{13/2}$ excited-state population density, L the length of the sample, and I_0 the incident pump intensity. The Fresnel reflection losses and the diffusion losses into the sample were included implicitly in I_0. It is worth noting that the real excited-state population N_2 is not homogeneous inside the sample due to the pump profile, so that in relation (2), N_2 represents in fact a mean value, which simplifies the calculations. On the other hand, the probe beam is wider than the pump one and, for each class of

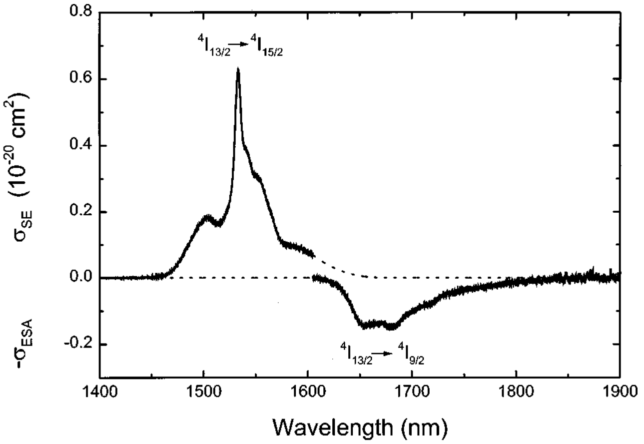

FIG. 6. SE and ESA spectra of Er^{3+} in phosphate glass (the resolution is 1 nm).

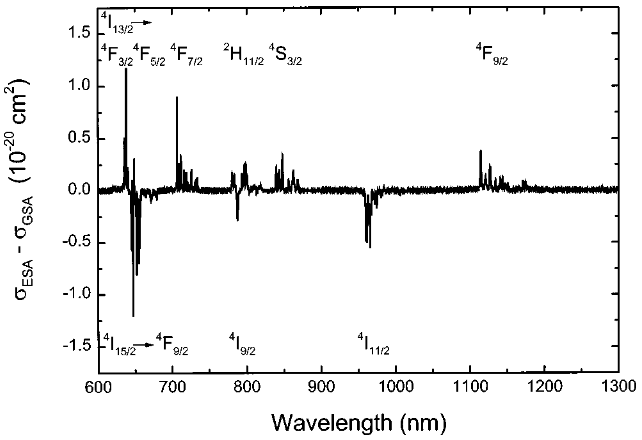

FIG. 8. Difference between ESA and GSA spectra of Er^{3+} in YAG (the resolution is 2 Å below 900 nm and 5 Å above).

optical rays i, the length crossed into the studied material may be decomposed into two parts: the first one, called the active length L_i, concerns the excited region and the second part, characterized by a length $L-L_i$ is not reached by the pump beam and contains only ions in the fundamental level.

Knowing that the use of the double modulation technique provides the mean transmission intensity $I_m=(I_{\text{on}}+I_{\text{off}})/2$ and the transmission variation $\Delta I=I_{\text{on}}-I_{\text{off}}$, and defining the ''transmission cross section'' $\sigma_T=\sigma_{\text{GSA}}+\sigma_{\text{SE}}-\sigma_{\text{ESA}}$, the $\Delta I/I_m$ ratio is written as

$$\frac{\Delta I}{I_m}=2\,\frac{-1+\Sigma_i\gamma_i e^{\sigma_T N_2 L_i}}{1+\Sigma_i\gamma_i e^{\sigma_T N_2 L_i}}. \tag{3}$$

Then, since the transmission variations induced by the pump are generally weak, we can use a first-order development and the ratio becomes

$$\frac{\Delta I}{I_m}\approx\sigma_T N_2 L^*, \tag{4}$$

where L^* is the mean transmission length of the sample ($L^*=\Sigma_i\gamma_i L_i$), and the measured signal is proportional to the transmission cross section:

$$\left(\frac{\Delta I}{I_m}\right)_{\text{exp}}=AN_2L^*\sigma_T, \tag{5}$$

where A is a coefficient due to the lock-in amplifiers. The value AN_2L^* cannot be calculated exactly but it can be determined experimentally. This coefficient is wavelength independent and can be determined from the ''excited-state absorption'' spectra in the spectral domains for which σ_{ESA} is negligible, and possibly for which σ_{SE} is also negligible, thus in which $\sigma_T=\sigma_{\text{GSA}}+\sigma_{\text{SE}}$ or $\sigma_T=\sigma_{\text{GSA}}$. σ_{GSA} is easily determined from the ground-state absorption spectra and the knowledge of the total dopant concentration. The stimulated cross-section σ_{SE} can be obtained from σ_{GSA}, in case of transitions involving the ground state, with the reciprocity formula[10]

$$\sigma_{\text{SE}}(\lambda)=\sigma_{\text{GSA}}(\lambda)\,\frac{Z_u}{Z_l}\exp\left(-\frac{hc}{kT}\left(\frac{1}{\lambda}-\frac{1}{\lambda_{ZL}}\right)\right), \tag{6}$$

where Z_u and Z_l are the partition functions for the upper and lower multiplets, respectively, and λ_{ZL} is the zero line wavelength of the transition between the lower Stark levels of these multiplets.

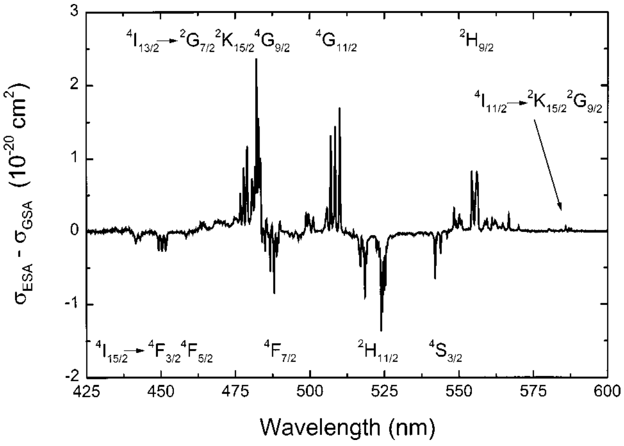

FIG. 7. Difference between ESA and GSA spectra of Er^{3+} in YAG (the resolution is 2 Å).

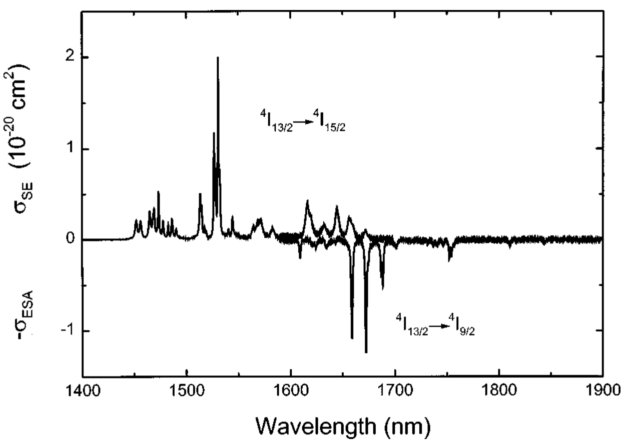

FIG. 9. SE and ESA spectra of Er^{3+} in YAG (the resolution is 5 Å).

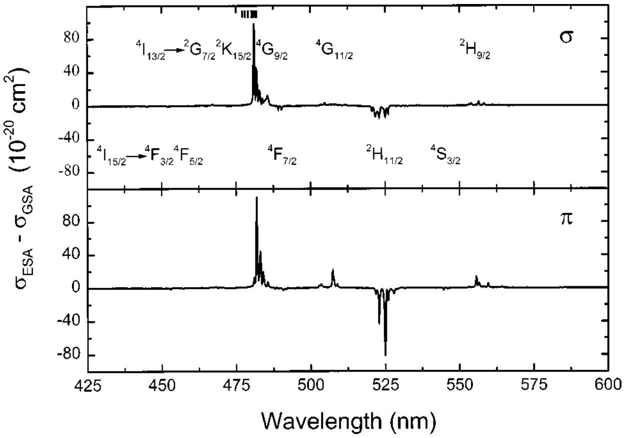

FIG. 10. Difference between ESA and GSA polarized spectra of Er^{3+} in YVO_4 (the resolution is 2 Å). The vertical bars indicate the positions of the lines expected by Ref. 12 for the $^4I_{13/2}\rightarrow{}^4G_{9/2}$ transition.

II. EXCITED-STATE ABSORPTION SPECTROSCOPY

The ESA spectra were registered between 400 and 3000 nm for Er^{3+}-doped YAG, YVO_4 and phosphate glass; they are reported in Figs. 4–13. Their spectral resolution depends on the wavelength range and is reported for each spectrum. During the measurements, slits with different widths were used to compensate for the response of the apparatus. Following the measurement, the first step was to evaluate the AN_2L^* coefficient introduced in expression (5). Most of the transitions from the ground state could not be used for this calibration because of their overlap with ESA transitions. In the visible range the transitions with very low or without such an overlap are $^4I_{15/2}\rightarrow{}^2H_{9/2}$ (~410 nm), $^2H_{11/2}$ (~525 nm), $^4F_{9/2}$ (~670 nm) and $^4I_{11/2}$ (~985 nm). The coefficient was then calculated by writting

$$AN_2L^* = \frac{\int \left(\frac{\Delta I}{I_m}\right)_{\exp} d\lambda}{\int \sigma_{\mathrm{GSA}} d\lambda}. \tag{7}$$

This coefficient was found not to be rigorously constant from one transition to the other and the most likely explanation is that the focal length of the lenses used in the experimental setup (which were not achromatic) may change significantly with the probe wavelength. Consequently, the light propagation into the sample may not be constant and leads to variations of the value of L^* as a function of the probe wavelength. As an example, we give in Table I the values of the AN_2L^* coefficient found for the phosphate glass (see Figs. 4 and 5): the mean value is $0.230\times10^{20}\,\mathrm{cm}^{-2}$ and the relative variation between about 400 and 1000 nm remains less than 10%. The $^4I_{15/2}\leftrightarrow{}^4I_{13/2}$ transition is the only one which can be used to derive the calibration coefficient for the IR region. Because this transition occurs in absorption and emission as well, expression (7) becomes

$$AN_2L^* = \frac{\int \left(\frac{\Delta I}{I_m}\right)_{\exp} d\lambda}{\int (\sigma_{\mathrm{GSA}} + \sigma_{\mathrm{SE}}) d\lambda}. \tag{8}$$

In this wavelength range the uncertainty is more important than in the visible range because of the uncertainty introduced by the calculated stimulated emission (SE) cross section, but it was estimated to be less than 20%.

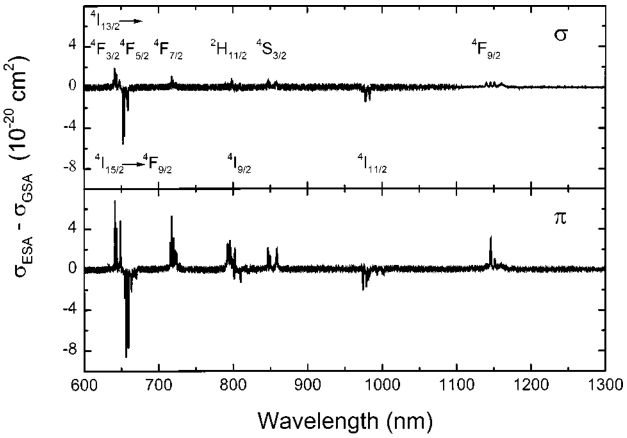

FIG. 11. Difference between ESA and GSA polarized spectra of Er^{3+} in YVO_4 (the resolution is 2 Å below 900 nm, 4 Å up to 1100 nm and 7 Å above).

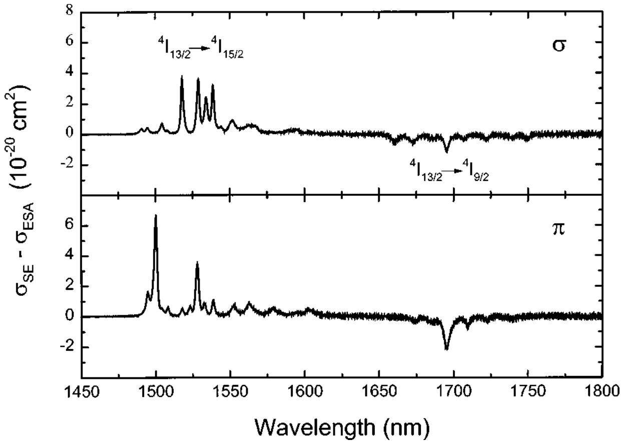

FIG. 12. Difference between SE and ESA polarized spectra of Er^{3+} in YVO_4 (the resolution is 7 Å).

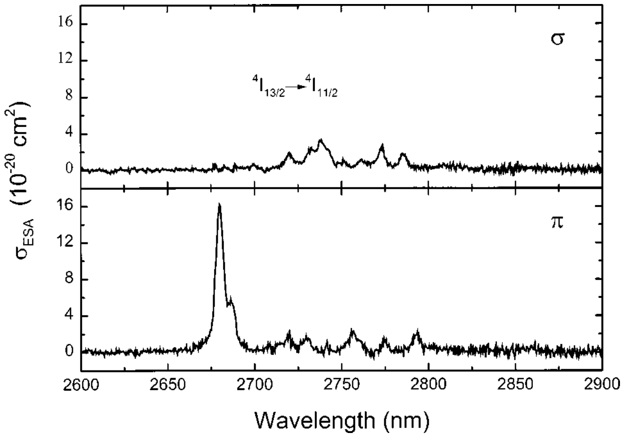

FIG. 13. ESA polarized spectra of Er^{3+} in YVO_4 (the resolution is 2 nm).

TABLE I. Different values of the AN_2L^* coefficient for Er^{3+}-doped phosphate glass.

Transition	Range (nm)	AN_2L^* ($10^{20}\ cm^{-2}$)
${}^4I_{15/2}\rightarrow{}^2H_{9/2}$	400–420	0.233
${}^4I_{15/2}\rightarrow{}^2H^{11/2}$	515–538	0.243
${}^4I_{15/2}\rightarrow{}^4F_{9/2}$	650–690	0.232
${}^4I_{15/2}\rightarrow{}^4I_{11/2}$	950–1020	0.213

TABLE II. Nonradiative energy-transfer microparameters of Er^{3+} in phosphate glass, YAG and YVO_4 in the 1.6-μm wavelength range. The Er:YVO_4 values have been averaged over the π and σ polarizations.

Sample	n	C_{DD} ($10^{-40}\ cm^6\ s^{-1}$)	C_{DA} ($10^{-40}\ cm^6\ s^{-1}$)
Phosphate glass	1.53	44	0.16
YAG	1.81	33	2.89
YVO_4	2.01	241	0

For Er^{3+}:YAG, the ESA spectrum was reported by Koetke and Huber[9] between 500 and 3000 nm by using a similar experimental setup. Our results reported in Figs. 7–9 are very close to theirs.

For all the studied materials, we observe that the ESA and GSA cross sections have the same order of magnitude. It is worth noticing, however, that the ${}^4I_{13/2}\rightarrow{}^4G_{9/2}$ ESA transition around 475 nm is very strong in the three materials and that the cross section of this transition almost reaches $10^{-18}\ cm^2$ in Er^{3+}:YVO_4.

The Stark sublevels positions are known for Er^{3+}:YAG (Ref. 11) and Er^{3+}:YVO_4,[12] in principle with good accuracy, so that the energies of the transitions between these Stark sublevels can be determined for any ESA transitions. As a matter of fact, except for the ${}^4I_{13/2}\rightarrow{}^4G_{9/2}$ ESA transition in YVO_4, a good general agreement it is found between the experimentally derived positions of the ESA transitions and those predicted assuming all these ESA transitions occur from the only ${}^4I_{13/2}$ metastable level to the upper energy levels, which justifies the assumption made at the beginning of Sec. I. In the case of the ${}^4I_{13/2}\rightarrow{}^4G_{9/2}$ ESA transition in YVO_4 (see Fig. 10), the Stark sublevels of the ${}^4G_{9/2}$ multiplet were obtained in fact theoretically by using crystal-field calculations.[12] According to the observed ESA lines, these Stark sublevels should lie at slightly lower energies. On the other hand, in the Er^{3+}:YAG visible ESA spectrum obtained after green excitation into the ${}^4S_{3/2}$ level, very weak lines are observed around 585 nm which cannot be explained by a transition originating from the ${}^4I_{13/2}$ level (see Fig. 7). The Stark levels analysis indicates in fact the possibility of a transition from the second ${}^4I_{11/2}$ excited level to the (${}^4G_{9/2}+{}^2K_{15/2}$) multiplet. In this crystal, the ${}^4I_{11/2}$ fluorescence lifetime is $\tau_{11/2}=100\ \mu s$ while that for the ${}^4I_{13/2}$ level is $\tau_{13/2}=6.5\ ms$,[13] so that, after ${}^4S_{3/2}$ excitation and relaxation of the excitation energy, we may consider that the ratio between the populations of the ${}^4I_{11/2}$ and ${}^4I_{13/2}$ levels should roughly follow that of their inverse fluorescence lifetimes and the population of ${}^4I_{11/2}$ would be approximately equal to about $\tau_{11/2}/\tau_{13/2}\sim 1.5\%$ that of ${}^4I_{13/2}$, which is small but not negligible. This type of transition is not observed in the two other materials, YVO_4, and the phosphate glass, due to their shorter ${}^4I_{11/2}$ fluorescence lifetimes, $\tau_{11/2}=27\ \mu s$ for Er^{3+}:YVO_4 (Ref. 12) and $\tau_{11/2}\sim 2.3\ \mu s$ for Er^{3+}:phosphate glass.[14]

III. INFLUENCE OF ESA ON LASER PROPERTIES

The most popular laser emission of the Er^{3+} ion in high phonon frequency materials is the quasi-four-level ${}^4I_{13/2}\rightarrow{}^4I_{15/2}$ laser emission around 1.6 μm. Consequently, population inversion is more easily achieved for transitions terminating on high-energy Stark levels of the ${}^4I_{15/2}$ ground-state multiplet, because of their reduced thermal populations. A low Er^{3+} dopant concentration is also needed to reduce reabsorption effects, so that the materials are often codoped with large amounts of Yb^{3+} ions, which absorb the excitation pump energy (provided by a high power diode laser operating around 970 nm, for example) and transfer it to the ${}^4I_{13/2}$ emitting level via the ${}^4I_{11/2}$ upper lying one after ${}^4I_{11/2}\rightarrow{}^4I_{13/2}$ nonradiative relaxation. Efficient laser emission in Yb, Er:phosphate glass for example is obtained for Yb^{3+} ion concentrations more than ten times larger than the Er^{3+} ion ones. Laser emission occurs at the maximum of the SE band near

TABLE III. Judd-Ofelt analysis of Er^{3+} in phosphate glass.

Transition ${}^4I_{15/2}\rightarrow$	Range (nm)	$\overline{\lambda}$ (nm)	$\int\sigma_{GSA}^{exp}d\lambda$ ($10^{-20}\ cm^2\ nm$)	$(\int\sigma_{GSA}d\lambda)^{JO}$ ($10^{-20}\ cm^2\ nm$)	$(\delta_{GSA})_i$ (%)
${}^4I_{13/2}$	1350–1750	1520.9	35.16	34.73	1.22
${}^4I_{11/2}$	930–1040	980.1	4.98	5.11	−2.61
${}^4I_{9/2}$	778–842	803.7	1.68	1.78	−5.95
${}^4F_{9/2}$	620–690	654.5	7.29	7.24	0.69
${}^4S_{3/2}$	537–560	545.2	1.39	1.18	15.11
${}^2H(2)_{11/2}$	500–537	521.7	20.83	20.84	−0.05
${}^4F_{7/2}$	470–502	488.3	3.71	3.87	−4.31
${}^4F_{5/2}+{}^4F_{3/2}$	435–465	449.6	1.21	1.54	−27.27
${}^2H(2)_{9/2}$	400–416	407.1	0.92	0.99	−7.61
Judd-Ofelt analysis:	$\Omega_2=5.81$ $\Delta_{GSA}=0.21\times10^{-20}\ cm^2\ nm$		$\Omega_4=1.49$	$\Omega_6=1.19$	($10^{-20}\ cm^2$)

TABLE IV. Judd-Ofelt analysis of Er^{3+} in YAG.

Transition $^4I_{15/2}\to$	Range (nm)	$\overline{\lambda}$ (nm)	$\int\sigma_{GSA}^{exp}d\lambda$ (10^{-20} cm^2 nm)	$(\int\sigma_{GSA}d\lambda)^{JO}$ (10^{-20} cm^2 nm)	$(\delta_{GSA})_i$ (%)
$^4I_{13/2}$	1350–1750	1497.5	25.08	24.88	0.80
$^4I_{11/2}$	900–1050	968.7	2.90	2.28	21.38
$^4I_{9/2}$	760–870	797.7	1.03	1.03	0.00
$^4F_{9/2}$	610–690	652.3	4.40	4.23	3.86
$^4S_{3/2}$	540–565	546.8	0.66	0.70	−6.06
$^2H(2)_{11/2}$	515–540	523.4	3.35	3.37	−0.60
$^4F_{7/2}$	472–502	488.4	1.86	2.30	−23.66
$^4F_{5/2}+^4F_{3/2}$	425–470	448.9	1.09	0.92	15.60
$^2H(2)_{9/2}$	400–420	408.3	0.56	0.60	−7.14
Judd-Ofelt analysis	$\Omega_2=0.39$		$\Omega_4=0.69$	$\Omega_6=0.55$	(10^{-20} cm^2)
	$\Delta_{GSA}=0.27\times10^{-20}$ cm^2 nm				

1543 nm,[15] nearly in coincidence with the ''zero line,'' and this laser emission could be tuned between 1525 and 1560 nm.[16] According to Fig. 6, ESA in this spectral domain is completely negligible and only overlaps ($^4I_{13/2}\to{}^4I_{9/2}$ ESA transition) with stimulated emission for wavelengths longer than 1600 nm which has no importance. In the case of Er^{3+}:YAG, the overlap between ESA and SE is more important (Fig. 9). No ESA line is found in coincidence with the main laser line reported at 1.64 μm.[17] However, as mentioned in Ref. 9, the emission peak at 1658 nm is affected by ESA losses and the one at 1673 nm is even prevented by ESA. In Er^{3+}:YVO_4, GSA and SE, on one hand, and ESA, on the other hand, do not overlap at all (see in Fig. 12) and laser emission could occur, in principle, at any wavelength in the gain region. Moreover, the SE cross sections in this crystal are substantially larger than in the other materials but, to our knowledge, no laser emission of Er:YVO_4 or of codoped Yb,Er:YVO_4 has been observed yet.

Another important Er^{3+} laser emission is that corresponding to the $^4I_{11/2}\to{}^4I_{13/2}$ transition around 2.8 μm. In principle, laser emission between the $^4I_{11/2}$ and $^4I_{13/2}$ energy levels is not favorable in oxide materials with high phonon frequencies, because of a reduced $^4I_{11/2}$ fluorescence quantum efficiency and of a lifetime of the terminal level of the transition which is longer than that of the emitting one. As a matter of fact, no laser emission has ever been reported nor is expected in Er:YVO_4 or Er:phosphate glass. However, the 2.94-μm laser emission of Er:YAG is very well known[18] and a number of laser devices based on this system are now commercially available, especially for medical applications. This was made possible by doping the YAG crystals very heavily, with more than 10 at. % Er^{3+}. Such a high dopant concentration indeed favors $(^4I_{13/2}+{}^4I_{13/2})\to(^4I_{15/2}+{}^4I_{9/2})$ $Er^{3+}-Er^{3+}$ energy transfers which depopulate and reduce the lifetime of the $^4I_{13/2}$ terminal level of the laser transition and repopulate the $^4I_{11/2}$ laser emitting state after nonradiative relaxation from the $^4I_{9/2}$ level. The laser emission through the $(^4I_{11/2}\to{}^4I_{13/2})$ transition is very improbable in YVO_4 and in phosphate glass for the following reasons: in Er^{3+}:YVO_4, the ESA $(^4I_{13/2}\to{}^4I_{9/2})$ and the SE $(^4I_{13/2}\to{}^4I_{15/2})$ transitions do not overlap so that the up-conversion process can only be phonon assisted. In this case the up-conversion will be inefficient to depopulate the lower laser level and repopulate the upper laser level. Concerning the phosphate glass, although the overlap between these transitions is not nil, the ratio of the two concerned lifetimes is such (see Sec. II) that the population inversion between the $^4I_{11/2}$ and $^4I_{13/2}$ levels cannot be reached.

TABLE V. Judd-Ofelt analysis of Er^{3+} in YVO_4.

Transition $^4I_{15/2}\to$	Range (nm)	$\overline{\lambda}$ (nm)	$\int\sigma_{GSA}^{exp}d\lambda$ (10^{-20} cm^2 nm)	$(\int\sigma_{GSA}d\lambda)^{JO}$ (10^{-20} cm^2 nm)	$(\delta_{GSA})_i$ (%)
$^4I_{13/2}$	1400–1700	1524.8	68.96	65.29	5.32
$^4I_{11/2}$	950–1030	984.4	9.96	11.32	−13.65
$^4I_{9/2}$	770–860	807.3	4.02	3.47	13.68
$^4F_{9/2}$	610–690	657.5	14.98	14.95	0.20
$^4S_{3/2}$	540–560	548.9	1.60	2.65	−65.63
$^2H(2)_{11/2}$	510–540	524.2	52.24	52.27	−0.06
$^4F_{7/2}$	470–510	491.3	7.19	8.67	−20.58
$^4F_{5/2}+^4F_{3/2}$	435–465	451.4	2.75	3.60	−30.91
$^2H(2)_{9/2}$	400–420	408.2	1.99	2.37	−19.10
Judd-Ofelt analysis:	$\Omega_2=9.42$		$\Omega_4=1.90$	$\Omega_6=1.69$	(10^{-20} cm^2)
	$\Delta_{GSA}=1.48\times10^{-20}$ cm^2 nm				

TABLE VI. Comparison between the measured integrated ESA cross sections and the ones derived from the Judd-Ofelt analysis for Er^{3+} in phosphate glass. Standard deviation: $\Delta_{ESA}=0.81\times 10^{-20}\,cm^2\,nm$. Quadratic average of the relative difference: $\overline{E}=15\%$. (Judd-Ofelt/experiment) ratio: $R=1.02$.

Transition $^4I_{13/2}\rightarrow$	Range (nm)	$\overline{\lambda}$ (nm)	$\int \sigma_{ESA}^{exp} d\lambda$ (10^{-20} cm^2 nm)	$(\int \sigma_{ESA} d\lambda)^{JO}$ (10^{-20} cm^2 nm)	$(\delta_{ESA})_i$ (%)
$^4I_{9/2}$	1600–1900	1692.6	13.44	13.83	−2.90
$^4F_{9/2}$	1100–1200	1141.6	3.61	3.99	−10.53
$^4S_{3/2}$	820–870	846.9	2.41	3.27	−35.68
$^2H(2)_{11/2}$	775–820	792.3	3.46	3.24	6.36
$^4F_{7/2}$	694–741	714.0	3.21	3.37	−4.98
$^4F_{5/2}+^4F_{3/2}$	607–675	639.9	3.94	4.29	−8.88
$^2H(2)_{9/2}$	541–567	554.4	5.11	5.47	−7.05
$^4G_{11/2}$	496–515	504.3	5.32	6.24	−17.29
$^4G_{9/2}+^2K_{15/2}+^2G(1)_{7/2}$	440–487	477.2	33.79	31.86	5.71

The third very interesting laser emission of the Er^{3+} ion is the one in the green associated with the $^4S_{3/2}\rightarrow{}^4I_{15/2}$ transition around 550 nm. This laser emission was already observed in Er^{3+}:YAG at 561 nm,[19] but again, as previously, nothing was observed and is even expected in Er^{3+} doped YVO_4 and phosphate glass. The effect of ESA on the laser emission of Er^{3+}:YAG was already reported in Ref. 2 so that we will only discuss here the two-photon pumping scheme proposed by Silversmith.[20] In this pumping scheme, the $^4S_{3/2}$ emitting level was reached by using two laser pump sources, one at $\lambda_1=812.9$ nm corresponding to the $^4I_{15/2}\rightarrow{}^4I_{9/2}$ GSA transition, and other at $\lambda_2=638.6$ nm corresponding to the ESA transition. This two-wavelength pumping is expected to improve the laser efficiency. The ESA spectrum reported in Fig. 8 indeed shows a very intense $^4I_{13/2}\rightarrow(^4F_{3/2}+^4F_{5/2})$ ESA transition at $\lambda_2=638.6$ nm with a cross section $\sigma_{ESA}=1.2\times 10^{-20}\,cm^2$. From the point of view of pumping efficiency, it seems also interesting to consider the $^4I_{15/2}\rightarrow{}^4I_{11/2}$ GSA transition around 980 nm as the first stage of this two-step absorption pumping scheme.

To conclude this section, it is worth noting that the laser diodes emitting around 650, 810, and 980 nm are well adapted for pumping Er^{3+} ions into their $^4F_{9/2}$, $^4I_{9/2}$, and $^4I_{11/2}$ levels, respectively. For the 1.6- and 2.9-μm laser emissions, the 980-nm radiation is the most interesting one because of large GSA cross sections and negligible ESA. It is also very useful to pump Yb, Er codoped systems.

IV. ENERGY-TRANSFER PARAMETERS

As mentioned above in the case of the 2.9-μm laser emission, energy transfers among the Er^{3+} active ions can be used advantageously. The efficiency of these energy transfers can be evaluated by calculating the energy-transfer microparameters introduced in the microscopic Förster-Dexter theory, assuming dipole-dipole interionic interactions.[5] In the case of the Er^{3+} ion various energy transfers can be considered.[13] Using our ESA measurements, two types of microparameters can be calculated: the donor-donor and the donor-acceptor microparameters labeled C_{DD} and C_{DA}, respectively. The donor-donor microparameter C_{DD} is related to migration-type energy transfers between Er^{3+} ions in which one ion in the $^4I_{13/2}$ metastable level transfers its energy to another one initially in its $^4I_{15/2}$ fundamental state. C_{DD} thus can be derived by calculating the overlap integral of the $^4I_{15/2}\leftrightarrow{}^4I_{13/2}$ ground-state absorption and emission cross-section spectra according to the expression[21]

TABLE VII. Comparison between the measured integrated ESA cross sections and the ones derived from the Judd-Ofelt analysis for Er^{3+} in YAG. Standard deviation: $\Delta_{ESA}=4.49\times 10^{-20}\,cm^2\,nm$. Quadratic average of the relative difference: $\overline{E}=21\%$. (Judd-Ofelt/experiment) ratio: $R=0.78$.

Transition $^4I_{13/2}\rightarrow$	Range (nm)	$\overline{\lambda}$ (nm)	$\int \sigma_{ESA}^{exp} d\lambda$ (10^{-20} cm^2 nm)	$(\int \sigma_{ESA} d\lambda)^{JO}$ (10^{-20} cm^2 nm)	$(\delta_{ESA})_i$ (%)
$^4I_{11/2}$	2500–3000	2709.1	62.01	48.65	21.54
$^4I_{9/2}$	1590–1860	1684.1	12.08	7.89	34.68
$^4F_{9/2}$	1105–1195	1137.6	2.79	1.99	28.67
$^4S_{3/2}$	830–875	851.4	1.91	1.92	−0.52
$^2H(2)_{11/2}$	770–830	804.6	2.38	2.10	11.76
$^4F_{7/2}$	701–750	715.8	1.96	1.98	−1.02
$^4F_{5/2}+^4F_{3/2}$	610–661	641.1	2.57	2.52	1.95
$^2H(2)_{9/2}$	547–575	561.4	2.85	2.06	27.72
$^4G_{11/2}$	491–521	506.8	2.75	2.37	13.82
$^4G_{9/2}+^2K_{15/2}+^2G(1)_{7/2}$	455–491	478.6	6.61	4.56	31.01

TABLE VIII. Comparison between the measured integrated ESA cross sections and the ones derived from the Judd-Ofelt analysis for Er^{3+} in YVO_4. Standard deviation: $\Delta_{\mathrm{ESA}}=14.40\times10^{-20}\,\mathrm{cm}^2\,\mathrm{nm}$. Quadratic average of the relative difference: $\overline{E}=22\%$. (Judd-Ofelt/experiment) ratio: $R=0.82$.

Transition $^4\mathrm{I}_{13/2}\rightarrow$	Range (nm)	$\overline{\lambda}$ (nm)	$\int\sigma_{\mathrm{ESA}}^{\mathrm{exp}}d\lambda$ ($10^{-20}\,\mathrm{cm}^2\,\mathrm{nm}$)	$(\int\sigma_{\mathrm{ESA}}d\lambda)^{\mathrm{JO}}$ ($10^{-20}\,\mathrm{cm}^2\,\mathrm{nm}$)	$(\delta_{\mathrm{ESA}})_i$ (%)
$^4\mathrm{I}_{11/2}$	2600–2900	2731.6	151.02	121.42	19.60
$^4\mathrm{I}_{9/2}$	1625–1800	1698.8	25.94	29.00	−11.80
$^4\mathrm{F}_{9/2}$	1100–1200	1147.7	9.68	8.14	15.91
$^4\mathrm{S}_{3/2}$	835–870	853.0	5.04	7.07	−40.28
$^2\mathrm{H}(2)_{11/2}$	780–835	798.9	8.26	6.28	23.97
$^4\mathrm{F}_{7/2}$	690–740	718.4	7.71	6.60	14.40
$^4\mathrm{F}_{5/2}+{}^4\mathrm{F}_{3/2}$	620–651	641.7	7.96	9.08	−14.07
$^2\mathrm{H}(2)_{9/2}$	540–570	557.5	14.37	12.82	10.79
$^4\mathrm{G}_{11/2}$	498–515	507.0	17.56	14.58	16.97
$^4\mathrm{G}_{9/2}+{}^2\mathrm{K}_{15/2}+{}^2\mathrm{G}(1)_{7/2}$	458–498	481.4	116.30	82.20	29.32

$$C_{DD}=\frac{3c}{8\pi^4n^2}\int\sigma_{\mathrm{GSA}}(\lambda)\sigma_{\mathrm{SE}}(\lambda)d\lambda. \tag{9}$$

The donor-acceptor microparameter C_{DA} necessary, for example, to evaluate the efficiency of the above mentioned $(^4\mathrm{I}_{13/2}+{}^4\mathrm{I}_{13/2})\rightarrow(^4\mathrm{I}_{15/2}+{}^4\mathrm{I}_{9/2})$ up-conversion energy transfer, is given by[21]

$$C_{DA}=\frac{3c}{8\pi^4n^2}\int\sigma_{\mathrm{ESA}}(\lambda)\sigma_{\mathrm{SE}}(\lambda)d\lambda, \tag{10}$$

an expression in which the overlap integral $\int\sigma_{\mathrm{ESA}}(\lambda)\sigma_{\mathrm{SE}}(\lambda)d\lambda$ concerns the involved $^4\mathrm{I}_{13/2}\rightarrow{}^4\mathrm{I}_{9/2}$ and $^4\mathrm{I}_{13/2}\rightarrow{}^4\mathrm{I}_{15/2}$ ESA and SE transitions, respectively.

These two microparameters C_{DD} and C_{DA} were calculated by using our cross-section spectra for the three materials and they are gathered in Table II.

The up-conversion energy transfer parameter C_{DA} thus derived in the case of Er:YAG and which is of interest for 2.94-μm laser emission is found to be $C_{DA}=2.89\times10^{-40}\,\mathrm{cm}^6\,\mathrm{s}^{-1}$. This value differs by three orders of magnitude from the value of $C_{DA}=1.7\times10^{-37}\,\mathrm{cm}^6\,\mathrm{s}^{-1}$ reported in the literature.[22] The latter was derived by using a rate equation model assuming two-dimensional energy transfers. This value is certainly too high; its order of magnitude is the one obtained in the case of resonant energy transfer and strong absorption and emission transitions, which is not the case. The discrepancy probably comes from the fact that these microscopic energy-transfer parameters cannot be simply derived from macroscopic rate equations. When migration is more important than the direct energy transfers, the macroscopic transfer coefficient W_{11}, used in population rate equations can be related to the microparameters[23] by the expression

$$W_{11}=\pi\left(\frac{2\pi}{3}\right)^{5/2}\sqrt{C_{DA}C_{DD}N_t}, \tag{11}$$

where N_t is the population in the $^4\mathrm{I}_{15/2}$ ground state. In Ref. 13, Georgescu *et al.* have found W_{11} equal to $1.7\times10^{-17}\,\mathrm{cm}^3\,\mathrm{s}^{-1}$ for $N_t=4.2\times10^{20}\,\mathrm{cm}^{-3}$. The value of W_{11} obtained using Eq. (11) with our microparameters is $0.82\times10^{-17}\,\mathrm{cm}^3\,\mathrm{s}^{-1}$. These two values of W_{11} are in rather good agreement if we consider the imprecision usually linked to the determination of this macroscopic parameter.

In the case of the Er:phosphate glass, the C_{DA} value is lower than in the case of Er:YAG due to the weak overlap between the considered emission and ESA transitions. Some ESA experiments performed with waveguide glasses were reported in Ref. 24. The ESA cross sections were determined from a JO analysis. Using their results, we could deduce the microparameters $C_{DA}=0.2\times10^{-40}\,\mathrm{cm}^6\,\mathrm{s}^{-1}$ for a barium silicate and $C_{DA}=1.0\times10^{-40}\,\mathrm{cm}^6\,\mathrm{s}^{-1}$ for an alumino-phosphosilicate glass. These values agree well with the value $C_{DA}=0.16\times10^{-40}\,\mathrm{cm}^6\,\mathrm{s}^{-1}$ found in our phosphate glass.

For Er:YVO_4, the ESA and SE cross-section spectra do not overlap at all (see Fig. 12) so that the associated C_{DA} value is practically equal to zero. Consequently, in this host, the up-conversion process will be very inefficient. Some estimate of C_{DA} could be found by including the vibronic sidebands of absorption and emission bands,[25] but this procedure would be certainly very approximative.

V. JUDD-OFELT ANALYSIS

Electric and magnetic dipole transitions constitute the main contribution to the optical spectra of the rare-earth ions in solids. Whereas the magnetic dipole (MD) line strengths can be easily calculated, the electric dipole (ED) transitions are forbidden between states belonging to the same electronic configuration. The ED transitions become partially allowed when odd terms of the crystal field mix opposite parity configuration states into $4f^n$. The crystal field is then considered as a perturbation of the free ion and ED and MD probabilities usually occur with the same orders of magnitude. Following the approach given by Judd[6] and Ofelt[7] it is possible to calculate the intensity of these ED transitions by making some approximations which are generally valid for the rare-earth ions. In this section, the Judd-Ofelt (JO) theory is applied to Er^{3+} in the studied matrices for transitions between the first excited-state level ($^4\mathrm{I}_{13/2}$) and the higher manifolds. Because a detailed description of the theory can be found for example in Ref. 1, only the main formula needed for the understanding are presented here. The line strength of the MD intermanifold $J\rightarrow J'$ transition is given by

$$S_{JJ'}^{\mathrm{MD}}=\left(\frac{h}{4\pi mc}\right)^2 |\langle 4f^n\alpha[SL]J\|\vec{L}+2\vec{S}\|4f^n\alpha'[S'L']J'\rangle|^2, \tag{12}$$

where $\vec{L}$ and $\vec{S}$ are the operators of the total orbital momentum and total spin, respectively. The reduced matrix element of the operator $\vec{L}+2\vec{S}$ were calculated using the eigenfunctions obtained by Weber.[26] In the JO theory, the ED line strength of the transition between the initial (J) and final (J') states is given by

$$(S_{JJ'}^{\mathrm{ED}})^{\mathrm{JO}}=\sum_{t=2,4,6}\Omega_t|\langle 4f^n\alpha[SL]J\|U^{(t)}\|4f^n\alpha'[S'L']J'\rangle|^2, \tag{13}$$

where $\langle 4f^n\alpha[SL]J\|U^{(t)}\|4f^n\alpha'[S'L']J'\rangle$ are reduced matrix elements of the unit tensor operator which depend only on the RE^{3+} ion because they are calculated with eigenfunctions of the free ion. In the present work, we used the matrix elements calculated by Kaminskii.[1] The intensity parameters Ω_t are characteristic of the ion-host combination and were determined from a least-square fit between the theoretical line strengths $(S_{JJ'}^{\mathrm{ED}})^{\mathrm{JO}}$ and those experimentally derived from the ground-state absorption spectra using the following relation:

$$(S_{JJ'}^{\mathrm{ED}})^{\mathrm{exp}}=\frac{9n}{(n^2+2)^2}\left(\frac{3hc(2J+1)\varepsilon_0}{2\pi^2e^2\overline{\lambda}}\int_{\lambda_1}^{\lambda_2}\sigma_{JJ'}(\lambda)d\lambda - nS_{JJ'}^{\mathrm{MD}}\right), \tag{14}$$

where $\sigma_{JJ'}$ stands for the absorption cross section, n is the refractive index of the host, and $\overline{\lambda}$ is the mean wavelength of the ${}^4\mathrm{I}_{15/2}\rightarrow J'$ absorption transition. The values of the refractive index were found in Refs. 1, 27, and 28 for YAG, phosphate glass, and YVO_4, respectively.

The results of the least-square fit to the absorption data for the spectra of Er^{3+} in phosphate glass, YAG, and YVO_4 between 400 and 1800 nm are reported in Tables III–V. In these tables, $\int\sigma_{\mathrm{GSA}}^{\mathrm{exp}}(\lambda)d\lambda$ stands for the measured integrated GSA cross section and $[\int\sigma_{\mathrm{GSA}}(\lambda)d\lambda]^{\mathrm{JO}}$ is the calculated value of this integrated cross section using the ED line strengths obtained with Eq. (13). $(\delta_{\mathrm{GSA}})_i$ is the relative difference between the experimental and the theoretical GSA integrated cross sections for each transition and Δ_{GSA} is the overall standard deviation:

$$\Delta_{\mathrm{GSA}}=\sqrt{\frac{\sum_{i=1}^{N}\{[\int\sigma_{\mathrm{GSA}}(\lambda)d\lambda]_i^{\mathrm{JO}}-[\int\sigma_{\mathrm{GSA}}^{\mathrm{exp}}(\lambda)d\lambda]\}^2}{N}}, \tag{15}$$

where N is the number of transitions or group of transitions taken into account in the least-square fit.

The intensity parameters are usually used to calculate the radiative transition probabilities, the radiative lifetimes, and the branching ratios for each transition. In our case, as aforesaid, the JO formalism allowed us to evaluate the ESA integrated cross sections and to compare them to the ones measured by using the experimental setup described previously. This comparison is presented in Tables VI, VII, and VIII for Er^{3+} in phosphate glass, YAG and YVO_4, respectively. The experimental ESA integrated cross sections $\int\sigma_{\mathrm{ESA}}^{\mathrm{exp}}(\lambda)d\lambda$ were determined after subtraction of the GSA and SE cross sections and the calculated ESA integrated cross sections $[\int\sigma_{\mathrm{ESA}}(\lambda)d\lambda]^{\mathrm{JO}}$ were calculated using expression (14). To make the comparison we have used $(\delta_{\mathrm{ESA}})_i$, the relative difference between experimental and theoretical ESA integrated cross sections for each transition, Δ_{ESA}, the overall standard deviation calculated with an expression similar to expression (15) and two new parameters, $\overline{E}$, the quadratic average of the relative difference

$$\overline{E}=\sqrt{\frac{\sum_{i=1}^{N}(\delta_{\mathrm{ESA}})_i^2}{N}} \tag{16}$$

and R, the ratio between the total theoretical and experimental integrated cross sections:

$$R=\frac{\sum_{i=1}^{N}[\int\sigma_{\mathrm{ESA}}(\lambda)d\lambda]_i^{\mathrm{JO}}}{\sum_{i=1}^{N}[\int\sigma_{\mathrm{ESA}}^{\mathrm{exp}}(\lambda)d\lambda]_i}. \tag{17}$$

$\overline{E}$ and R are thought to be more indicative of the agreement quality than the overall standard deviation Δ_{ESA} which mainly reflects the contribution of the most intense ESA transitions. However, the values of Δ_{ESA} are given for information.

For Er^{3+}-doped phosphate glass (Table VI), the integrated cross sections obtained by the JO analysis are in good agreement with the measured ones and the relative difference $(\delta_{\mathrm{ESA}})_i$ between them is always smaller than 20% with one exception: the small intensity transition ${}^4\mathrm{I}_{13/2}\rightarrow{}^4\mathrm{S}_{3/2}$ which is obtained with the worst experimental precision. The experimental and calculated total integrated cross sections are very close, with $R=1.02$ and $\overline{E}=15\%$. These results are good if we consider that the ESA cross sections are measured with an accuracy approximately equal to 20%. The values of the calculated cross sections for Er^{3+}:YAG (Table VII) are comparable to the measured ones and in the worst case, $(\delta_{\mathrm{ESA}})_i$ is equal to 35%. $\overline{E}$ remains close to 20% but the ratio R is only 0.78. For Er^{3+}:YVO_4 the calculated and measured ESA cross sections are also in good agreement (Table VIII) and the maximum relative difference is found for the already mentioned low intensity ${}^4\mathrm{I}_{13/2}\rightarrow{}^4\mathrm{S}_{3/2}$ transition ($\delta_{\mathrm{ESA}}\sim 40\%$). The quadratic average of the relative difference is comparable to the ones obtained for the other samples ($\overline{E}=22\%$) and like in YAG the calculated integrated cross sections seem to be systematically smaller than the experimental ones ($R=0.82$).

One explanation for the last point could be a saturation effect in the transmission spectra of the Er^{3+}-doped materials exhibiting intense and sharp lines like Er:YAG and Er:YVO_4. On the other hand, some ESA transitions overlap with GSA and the subtraction of the GSA cross sections may induce some additional imprecision on the values of the ESA integrated cross sections. It is apparently not the case if we consider in Tables VI–VIII the relative differences related to the ESA ${}^4\mathrm{I}_{13/2}\rightarrow{}^2\mathrm{H}_{11/2}$, ${}^4\mathrm{F}_{5/2}$, and ${}^4\mathrm{G}_{9/2}$ transitions that are the most concerned by the overlap with GSA transitions. At last, in the way the Ω_t parameters are calculated, several

$(\delta_{\rm GSA})_i$ values can be found which are larger than 20%. So, when these JO parameters are used to calculate the ESA cross sections, it is quite understandable that $(\delta_{\rm ESA})_i$ values of the same order of magnitude as $(\delta_{\rm GSA})_i$ are obtained.

CONCLUSION

The main advantage of the ESA experimental setup used in this work, based on the double modulation of the pump and probe beams, is to get rid of the fluorescence signal. The ESA spectra of Er^{3+} in YAG, YVO_4, and phosphate glass have been registered in the visible as well as in the IR regions up to 3 μm and the accuracy of these measurements is estimated to be better than 20% in all cases. The positions of the ESA transitions have been compared to those predicted from the Er^{3+} Stark sublevels found in the literature and a general good agreement is found. This comparison has revealed that the calculated positions of the Stark sublevels of the $^4G_{9/2}$ manifold in YVO_4 (Ref. 12) were not correct. The influence of ESA on the laser properties of the studied materials has been analyzed. Around 1.6 μm ($^4I_{13/2} \rightarrow {}^4I_{15/2}$ laser transition), Er:YAG is the only one to be affected by ESA losses. Concerning the potential laser operation through the $^4S_{3/2} \rightarrow {}^4I_{15/2}$ channel using a two-photon pumping scheme,[20] our measurements have confirmed the importance of ESA at 638.6 nm ($^4I_{13/2} \rightarrow {}^4F_{3/2} + {}^4F_{5/2}$ transition) as second step in the pumping scheme. The microparameters C_{DD} and C_{DA} related to the migration and up-conversion energy transfers involved in the 2.9-μm laser emission were calculated using our measured GSA, SE, and ESA cross sections. In Er:YAG, the value $C_{DA} = 2.89 \times 10^{-40}\ \mathrm{cm}^6\,\mathrm{s}^{-1}$ deduced from our data seems much more realistic than the one found in the literature.[22] Finally, the JO formalism has been used to estimate the ESA integrated cross sections from the $^4I_{13/2}$ manifold and the results compare well with the experimentally derived values: the accuracy of these Judd-Ofelt predictions lies within 20%, which is also typical of the predictions in the case of the ground-state absorption data.

ACKNOWLEDGMENTS

Thanks are expressed to D. Ritz (FEE, Idaroberstein, Germany) and Z. Frukacz (ITME, Warsaw, Poland) for providing us with the Er:YVO_4 and Er:YAG crystals, respectively.

---

*FAX: (33) 2 31 45 25 57. Electronic address: doualan@spalp255.ismra.fr

[1] A. A. Kaminskii, *Crystalline Lasers: Physical Processes and Operating Schemes* (CRC, Boca Raton, 1996).

[2] T. Danger, J. Koetke, R. Brede, E. Heumann, G. Huber, and B. H. T. Chai, J. Appl. Phys. **76**, 1413 (1994).

[3] F. Auzel, in *Radiationless Processes*, edited by B. Di Bartolo, Series B: Physics Vol. B62 (Plenum, New York, 1980), pp. 213–286.

[4] S. A. Pollack, D. B. Chang, M. Birnbaum, and M. Kokta, J. Appl. Phys. **70**, 7227 (1991).

[5] D. L. Dexter, J. Chem. Phys. **21**, 836 (1953).

[6] B. R. Judd, Phys. Rev. **127**, 750 (1962).

[7] G. S. Ofelt, J. Chem. Phys. **37**, 511 (1962).

[8] Y. Guyot and R. Moncorgé, J. Appl. Phys. **73**, 8526 (1993).

[9] J. Koetke and G. Huber, Appl. Phys. B: Lasers Opt. **61**, 151 (1995).

[10] S. A. Payne, L. L. Chase, L. K. Smith, W. L. Kway, and W. F. Krupke, IEEE J. Quantum Electron. **28**, 2619 (1992).

[11] J. B. Gruber, J. R. Quagliano, M. F. Reid, F. S. Richardson, M. E. Hills, M. D. Seltzer, S. B. Stevens, C. A. Morrison, and T. H. Allik, Phys. Rev. B **48**, 15 561 (1993).

[12] J. A. Capobianco, P. Kabro, F. S. Ermeneux, R. Moncorgé, M. Bettinelli, and E. Cavalli, Chem. Phys. **214**, 329 (1997).

[13] S. Georgescu, V. Lupei, A. Lupei, V. I. Zhekov, T. M. Murina, and M. I. Studenikin, Opt. Commun. **81**, 186 (1991).

[14] P. Le Boulanger, Ph.D. dissertation, Laboratoire de Spectroscopie Atomique, ISMRA, Université de Caen, France, 1998.

[15] E. Snitzer and R. Woodcock, Appl. Phys. Lett. **6**, 45 (1965).

[16] A. A. Petrov and V. A. Fromzel, Opt. Spektrosk. **70**, 1098 (1991) [Opt. Spectrosc. **70**, 643 (1991)].

[17] H. Stange, K. Petermann, G. Huber, and E. W. Duczynski, Appl. Phys. B: Photophys. Laser Chem. **49**, 269 (1989).

[18] E. V. Zharikov, V. I. Zhekov, L. A. Kulevskii, T. M. Murina, V. V. Osiko, A. M. Prokhorov, A. D. Savel'ev, V. V. Smirnov, B. P. Starikov, and M. I. Timoshechkin, Kvant. Elektron. (Moscow) **1**, 1867 (1974) [Sov. J. Quantum Electron. **4**, 1039 (1975)].

[19] R. Brede, E. Heumann, J. Koetke, T. Danger, G. Huber, and B. Chai, Appl. Phys. Lett. **63**, 2030 (1993).

[20] A. Silversmith, J. Lumin. **60–61**, 636 (1994).

[21] J. A. Caird, A. J. Ramponi, and P. R. Staver, J. Opt. Soc. Am. B **8**, 1391 (1991).

[22] J. Wang and D. J. Simkin, Phys. Rev. B **52**, 3309 (1995).

[23] A. I. Burshtein, Zh. Eksp. Teor. Fiz. **62**, 1695 (1972) [Sov. Phys. JETP **35**, 882 (1972)].

[24] J. E. Roman, M. Hempstead, C. Ye, S. Nouh, P. Camy, P. Laborde, and C. Lerminiaux, Appl. Phys. Lett. **67**, 470 (1995).

[25] F. Auzel, Phys. Rev. B **13**, 2809 (1976).

[26] M. J. Weber, Phys. Rev. **157**, 262 (1967).

[27] *Glass Laser Rods* (Kigre, Inc., Hilton Head, 1990).

[28] *Crystals* (Fujian Castech Crystals, Inc., Fujian, China, 1996).